Nano Research

Open Access

Research Article

Tuning Lewis acid in nickel-containing polyoxometalates for enhanced ethanol selectivity of methane electrooxidation reactions

Jvwei Liu[1], Qiang Zhang[1,2]✉, Conglin Chen[1], Shenjie Zhang[1], Jiaxin Jiang[1], and Junqiang Xu[3]

[1] *School of Chemistry & Chemical Engineering, Chongqing University of Technology, Chongqing 400054, China*
[2] *National Engineering Laboratory for Methanol to Olefins, Dalian National Laboratory for Clean Energy, iChEM (Collaborative Innovation Center of Chemistry for Energy Materials), Dalian Institute of Chemical Physics, Chinese Academy of Sciences, Dalian 116023, China*
[3] *Yangtze Normal University, Chongqing 408100, China*

Cite this article: *Nano Research*, **2026**, *19*, 94908604. https://doi.org/10.26599/NR.2026.94908604

ABSTRACT: The electrocatalytic oxidation of methane (CH_4) facilitates the direct conversion of abundant natural gas into value-added chemicals utilizing renewable electricity. However, the high dissociation energy of the C–H bond and the presence of multiple competing reaction pathways lead to poor product selectivity. We synthesized a Ni-based polyoxometalate (Ni-POM-V_O) through cluster-nucleus co-assembly and introduced rich oxygen vacancies using N_2 cold plasma etching. The optimized catalyst attained a Faradaic efficiency of 88.4% for ethanol at 1.7 V versus the reversible hydrogen electrode (RHE). Notably, the oxygen vacancies in Ni-POM-V_O create Lewis acid sites that enhance methane adsorption and activation, thereby facilitating its conversion into $*CH_2$ and $*CH_2OH$ intermediates. The subsequent adsorption of these intermediates onto the polyoxometalate (POM) framework promotes C–C coupling, resulting in ethanol production. This work provides a new method for adjusting the Lewis acid content on the catalyst surface through oxygen vacancies, improving the selectivity of methane electro oxidation to ethanol.

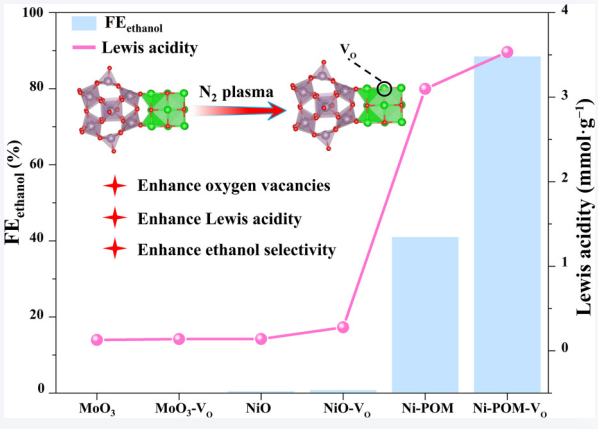

KEYWORDS: Lewis acid, polyoxometalates (POMs), oxygen vacancy, methane electrooxidation, selectivity

1 Introduction

The electrochemical oxidation of methane (CH_4OR) to produce high-value chemicals (e.g., methanol, ethanol, and acetic acid) represents one of the most economically promising objectives in the chemical industry [1–3]. Currently, methane oxidation predominantly yields C1 products, whereas the selective conversion to more valuable C_{2+} products remain challenging [4]. This challenge stems from the highly symmetric tetrahedral structure of methane and the exceptional stability of its C–H bond (439.3 kJ·mol^{-1}). Effective conversion of methane requires catalysts with adequate activity to cleave the C–H bond; however, excessive catalytic activity can lead to over-oxidation of products. Therefore, achieving an optimal balance between catalytic activity and product selectivity is a significant challenge [5]. Furthermore, existing catalysts are constrained by their inability to stabilize crucial reaction intermediates, which is essential for selective C–C coupling [6, 7].

Nickel-based catalysts are extensively utilized for methane oxidation [8, 9]. Various oxidation states of nickel exhibit distinct roles in methane electrocatalysis. It is widely accepted that the Ni^0 active site efficiently adsorbs and activates CH_4 [10]. The Ni^{2+} active center exhibits a strong adsorption capacity for the crucial $*CH_3$ species, influencing the selectivity of the CH_4 oxidation reaction (CH_4OR) towards C_2 products. For instance, the Ni^{2+}/Ni^0 interface catalysts act as active centers for the electrooxidation of CH_4 to alcohols, achieving a high Faraday efficiency for ethanol (89% at 1.40 V, 25 μmol·g^{-1}·h^{-1}) [11]. Despite the significant attention that Ni-based catalysts have received due to their tunable d-electronic structures and the formation of NiOOH active phases in alkaline media, their intrinsic lattice oxygen sites often restrict effective contact between the organic substrate and the metal active centers. This limitation adversely affects the reaction rate and current density, particularly in polyol oxidation and other processes involving complex C–C bond cleavage, resulting in poor activity

Received: September 2, 2025; **Revised:** February 2, 2026
Accepted: February 25, 2026

✉Address correspondence to zqiang@cqut.edu.cn

and selectivity. Drawing inspiration from the mechanism of ligand microenvironmental regulation [12, 13], this study employs a metal-polyoxometalates ligand design approach. This method addresses the fundamental issue of limited active site exposure in conventional Ni-based materials.

Polyoxometalates (POMs) represent a distinct class of anionic metal oxides that have significant applications in energy conversion, molecular catalysis, bionics, and therapeutic diagnostics [14–18]. To date, various POM-based materials, such as POM clusters, POM@MOFs, and M-POM, have been developed and effectively utilized in photo/electrocatalytic CO_2 reduction reaction (CO_2RR), hydrogen evolution reaction (HER), and oxygen evolution reaction (OER) [19–22]. Recent studies have conclusively demonstrated that oxygen vacancies formed on the POM surface serve as active sites for methane thermal activation, facilitating aerobic methane oxidation [23, 24]. Furthermore, this system has been extended to the thermoelectrocatalytic conversion of methane. By utilizing reduced PTA to initiate thermocatalysis in the solution phase, it resolves the kinetic issue of slow methane oxidation and prevents peroxidation on the electrode surface [25]. Traditional POM-based clusters, characterized by saturated metal-centered coordination spheres, exhibit limited catalytic activity and are infrequently utilized for methane electrooxidation. To address this issue, the incorporation of NiO into POM facilitated enhanced activation of the C–H bond. The resulting *COOH intermediate was stabilized by off-domain electrons within the POM clusters. The sequential active sites of NiO and POM at the molecular level facilitated the *in situ* coupling of *COOH to oxalates. The photoelectrochemical coupling of methane to produce C_2 products under mild conditions demonstrated excellent catalytic activity, achieving a remarkable productivity of up to 4.48 $mmol \cdot g_{cat}^{-1} \cdot h^{-1}$ and high selectivity (> 99%) [26]. Improving the conversion of methane to C_{2+} products under mild conditions necessitates not only promoting methane activation but also facilitating C–C coupling among the reaction intermediates. Research has shown that Lewis acid sites enhance the adsorption and activation of methane, facilitating its conversion to $*CH_3$ and $*CH_2$ intermediates. Additionally, by introducing or adjusting Lewis acid sites, the catalyst can stabilize the intermediate structure and reduce the activation energy of the reaction, thereby further promoting the C–C coupling reaction [27].

Lewis acid–base sites are crucial in catalysis, particularly for regulating reaction pathways and enhancing selectivity and activity [28–30]. Lewis acid sites are able to accept electron pairs, typically found in electron-deficient metal centers or cations. Transition metals, such as Fe, Co, Ni, and Pt, exhibit Lewis acidity because of their unfilled orbitals [31–33]. Lewis acid sites can adsorb substrates with lone electron pairs (e.g., CO, NH_3, and CH_4), thereby enhancing catalytic activity. Additionally, they can modulate the reaction pathway to minimize side reactions and alter electron distribution at the metal center, optimizing the catalyst's activity and stability. For instance, the single-atom Cu catalyst, based on Lewis acid, facilitates the electrocatalytic reduction of CO_2 to produce CH_4. Theoretical calculations demonstrated that Lewis metal oxides (e.g., Al_2O_3, Cr_2O_3) can modulate the electronic structure of Cu atoms by optimizing intermediate adsorption, thereby facilitating CO_2 methanation [34].

Furthermore, Lewis acid or base sites can form from defective sites on the carrier [35]. One such defect is oxygen vacancies, whose formation is associated with the emergence of ligand-unsaturated metal sites, typically acting as Lewis acid active centers. Oxygen vacancies (V_O) and carbon defects (D_C) were generated in $Ni/CeO_2/C$ catalysts via an *in-situ* calcination-induced etching method. The abundant oxygen vacancies (acting as Lewis acidic sites) and carbon defects (serving as Lewis basic sites) collaborated to create numerous heterogeneous hindered Lewis acid-base pair active sites on $Ni/CeO_2/C$ catalysts, enhancing the CTHDO reaction of lignin oil and its derivatives [36]. Numerous studies indicate that Lewis acid sites can influence the reaction pathway and improve product selectivity [37]. Nevertheless, controlling a greater number and stronger Lewis acid sites in catalysts remains a significant challenge.

Herein, we report the preparation of Ni-POM-V_O catalysts using a cluster-nucleus co-assembly strategy. The Ni-POM-V_O structure, which is rich in oxygen vacancies, facilitates the generation of a greater number of Lewis acid sites, thereby enhancing product selectivity. Ni-POM-V_O demonstrates exceptional catalytic activity for CH_4OR and achieves a high ethanol selectivity of 88.4%. Its performance surpasses that of previously reported electrocatalysts under room temperature and ambient pressure conditions [38–44]. During the reaction, oxygen vacancy defects with significant Lewis acid activity enhance the adsorption and activation of methane, leading to the subsequent conversion into $*CH_3$ and $*CH_2$ intermediates. The further adsorption of $*CH_3$ and $*CH_2$ on POM facilitates the C–C coupling reaction, resulting in ethanol production. H_2O molecular can be oxidized to *OH through the cavities in POM, effectively stabilizing reaction intermediates ($*CH_3$, $*CH_2$, and $*CH_2OH$) to facilitate ethanol production and release while inhibiting its peroxidation to CO_2. This strategy, which involves adjusting both the concentration and type of Lewis acids on the catalyst surface by manipulating oxygen vacancy concentrations, offers novel insights for electro-oxidation synthesis reactions.

2 Experimental

2.1 Synthesis of Ni-POM

The steps to synthesize Ni-POM were as follows: First, 1 mmol of $(NH_4)_6Mo_7O_{24} \cdot 4H_2O$ was dissolved with 20 mL of pure water, followed by the addition of 1.0 g of polyvinyl pyrrolidone (PVP), and 1.8 mmol of $NiCl_2 \cdot H_2O$ was added under continuous stirring conditions. The above mixture was stirred at room temperature for 2 h, then 5 mL, 0.6 mmol $NH_4H_2PO_4$ was quickly added and stirred at 80 °C for 4 h, 50 mL ethanol was added for alcohol precipitation, and then washed with water and ethanol three times. The precipitates were dried in vacuum at 50 °C, and the resulting dry powder was Ni-POM.

2.2 Synthesis of NiO

The synthesis of NiO involved several key steps. First, 5 mmol of $Ni(NO_3)_2 \cdot 6H_2O$ and urea were weighed and dissolved in a mixture of 25 mL of ethylene glycol and 5 mL of deionized water, resulting in a green solution upon complete dissolution. The resulting mixed solution was then transferred to a PTFE-lined stainless steel autoclave, where it was maintained at 180 °C for 10 h. Afterward, the solution was allowed to cool naturally to room temperature, washed three times with deionized water and ethanol, and subsequently dried in an oven at 50 °C. The dried powder was calcined in air at 350 °C for 4 h, ultimately yielding NiO powder.

2.3 Synthesis of MoO_3

The synthesis of MoO_3 involved several steps: First, 4.950 g of $(NH_4)_6Mo_7O_{24}{\cdot}4H_2O$ was weighed and dissolved in 20 mL of deionized water. Next, 10 mL of nitric acid was added slowly while stirring. The mixture was then transferred to an oil bath and heated at 120 °C for 3 h. After heating, the mixture was cooled to room temperature, centrifuged, and washed with deionized water and ethanol. The resulting precipitate was then dried under vacuum at 70 °C for 7 h. Finally, the dried powder was calcined at 600 °C for 5 h to obtain MoO_3 powder.

2.4 Synthesis of Ni-POM-V_O, NiO-V_O and MoO_3-V_O

The Ni-POM particles were subjected to plasma treatment at a power of 200 W for 20 min in a nitrogen atmosphere to prepare Ni-POM-V_O. The pressure was 20 Pa, and the gas flow rate was 10 sccm. Additionally, NiO-V_O and MoO_3-V_O were synthesized under the same conditions.

2.5 Characterization

The crystallinity and spatial configuration of the catalysts were analyzed using X-ray diffraction spectroscopy with a graphite monochromator. The specific test conditions included the use of Cu Kα rays as the excitation source, an accelerating tube voltage of 40 kV, a tube current of 40 mA, a scanning range of 2θ = 10°–90°, and a scanning speed of 5 °/min. N_2 adsorption–desorption isotherms of the catalysts were conducted at 77 K using a JW-BK132F device to obtain surface area parameters, pore volume, and pore size distribution. Additionally, the specific surface area and pore size distribution of the samples were calculated using the classical Brunauer–Emmett–Teller (BET) and Barrett–Joyner–Halenda (BJH) models, respectively. The BSD-C200 automated chemical adsorption analyzer was utilized for NH_3 programmed temperature resolution analysis to assess catalyst surface acidity and ammonia adsorption capacity. A 60 mg sample of the catalyst was kept in a helium atmosphere at 300 °C for 60 min, then cooled to 50 °C and exposed to a 5% NH_3/He mixture for another 60 min. Finally, the catalyst was heated at a rate of 10 °C·min^{-1} in a helium atmosphere from 50 to 800 °C for NH_3 temperature-programmed desorption (NH_3-TPD) testing. The same apparatus was employed for CH_4 temperature-programmed desorption (CH_4-TPD) testing as was used for NH_3-TPD, except during the gas switching phase. The elemental composition of the catalyst surface was analyzed using X-ray photoelectron spectroscopy (XPS, ESCA-LAB250Xi) under Al-Kα radiation (15 kV, 30 mA). The morphology and composition of the catalysts were analyzed using transmission electron microscopy (TEM, SM-7800F) coupled with energy dispersive X-ray spectroscopy (EDX).

2.6 Electrochemical measurement for CH_4 oxidation

CH_4OR was conducted in a standard three-electrode system utilizing a 0.1 M KOH solution (298 K, pH = 13) as the electrolyte, housed within an airtight two-chamber electrochemical cell separated by a Nafion-212 membrane. The experimental setup included a platinum counter electrode, a calomel reference electrode, and a glassy carbon working electrode, with a CHI-660E electrochemical workstation. Initially, 4.2 mg of catalyst and 5 μL of 5 wt.% Nafion solution were added to 395 μL of isopropanol and sonicated for 10 min to produce a catalyst slurry. The slurry was then evenly applied onto the surface of the glassy carbon electrode (area = 0.07 cm^2), with a catalyst loading of approximately 0.7 mg·cm^{-2}, and allowed to dry naturally to form the working electrode. The electrolyte was purged with high-purity Ar (99.999%) for 30 min to eliminate impurities, after which high-purity CH_4 (99.99%) was injected to create a saturated CH_4 solution. The catalytic activity of the catalyst was assessed using cyclic voltammetry (CV) and linear sweep voltammetry (LSV). The stability of the catalyst was examined through chronoamperometry. The electrochemical impedance of the catalyst was examined using electrochemical impedance spectroscopy (EIS) with a frequency range of 1–10^6 Hz, a potential of 1.7 V vs. RHE, and an amplitude of 5 mV. The electrode potentials were converted into reversible hydrogen electrode by the equation (Eq. (1))

$$E\,(\text{vs. RHE}) = E\,(\text{vs. Hg/Hg}_2\text{Cl}_2) + 0.241\ \text{V} + 0.059 \times \text{pH} \quad (1)$$

2.7 Product detection

Gaseous products were detected using a gas chromatograph (SC3000B) equipped with a TDX01 molecular sieve column, with measurements taken at 30-min intervals. The composition of the liquid sample was analyzed using nuclear magnetic resonance (NMR) spectroscopy. For NMR sample preparation, 0.1 mL of D_2O containing 0.05 mL of dimethyl sulfoxide served as the internal standard. After the electrolytic reaction, 0.1 mL of electrolyte was combined with the internal standard solution for NMR analysis. Faraday efficiency and conversion frequency were calculated by measuring the product yield and current during the reaction under constant potential for 2 h. Based on the product measurements, the Faraday efficiency (FE) was calculated by measuring the products of the reaction and the current values after 6 h of reaction at a constant potential. The Faraday efficiency is calculated as the ratio of the amount of charge used in the conversion of CH_4 products to the amount of charge flowing per unit time (Eq. (2))

$$\text{FE}_{\text{ethanol}} = \frac{n_{\text{ethanol}} \times N \times F}{I \times t} \times 100\% \quad (2)$$

where n is the amount of product, N is the number of electrons involved in the reaction, FE is the Faraday efficiency, and I is the current.

2.8 Density functional theory calculations

All DFT calculations were performed using the CASTEP and DMol^3 packages with ultrasoft potentials (USP) to account for electron-ion interaction. The electron–electron connection and van der Waals interaction were modeled using generalized gradient approximation (GGA) in the Perdew–Burke–Ernzerhof (PBE) and DFT-D2 methods. The Bril louin zone integral was evaluated using a Monkhorst–Pack (MP) grid of special points with a 3 × 3 × 3 k-point grid. The convergence limit for the electronic self-consistent field loop was set at 1 × 10^{-6} eV·atom^{-1}. The residual force on the atomic structure was minimized to below 0.05 eV. Cell parameters were optimized using the finite basis correction approach to ensure a stress less than 0.1 GPa. All atom positions were relaxed without imposing symmetry limitations.

3 Results and discussion

3.1 Morphological and structural analysis

The preparation process for Ni-POM-V_O is illustrated in Fig. 1(a). Ni-POM was synthesized via cluster-nucleus co-assembly, in which

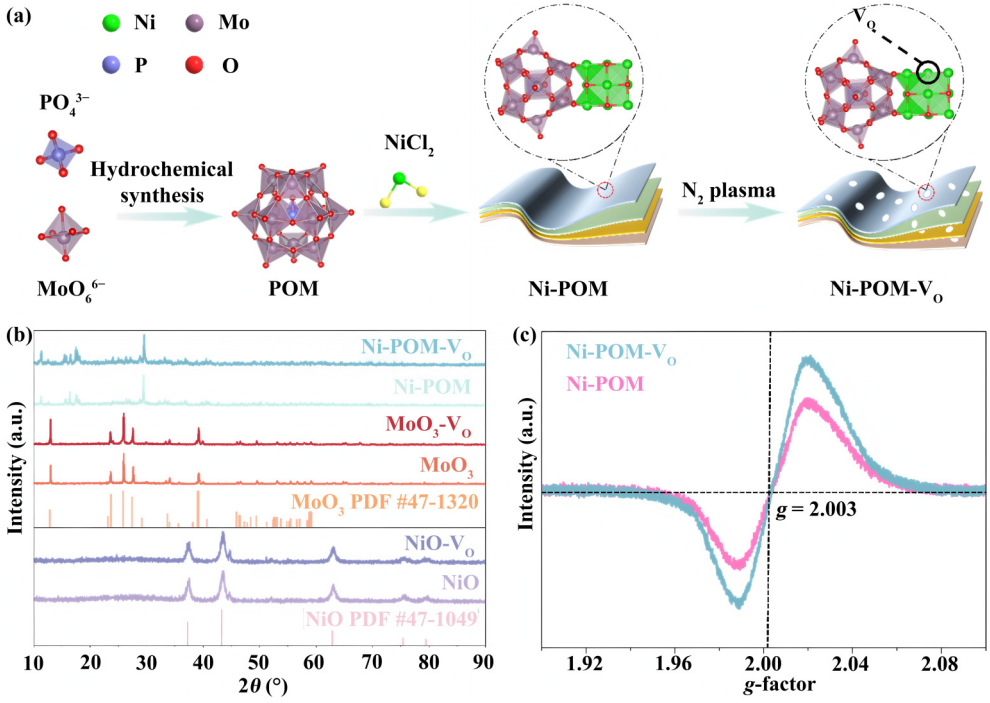

Figure 1 (a) Schematic illustration of the Ni-POM-V_O preparation process. (b) XRD patterns of all catalysts. (c) EPR spectra of Ni-POM and Ni-POM-V_O.

PO_4^{3-} and MoO_6^{6-} clusters were combined with Ni nuclei through direct bonds between the heterounits. Subsequently, the Ni-POM precursor was etched using N_2 plasma to produce Ni-POM enriched with oxygen vacancies, denoted as Ni-POM-V_O. To further elucidate the crystal structure of Ni-POM-V_O, XRD analysis was conducted, with the corresponding diffraction patterns presented in Fig. 1(b). For comparative structural analysis, reference samples of MoO_3 and NiO were synthesized. The diffraction peaks of the as-prepared MoO_3 and NiO align well with the standard reference patterns (MoO_3 PDF #47-1320 and NiO PDF #47-1049), confirming their successful preparation. Notably, no characteristic peaks corresponding to MoO_3 or NiO were observed in the XRD pattern of Ni-POM, suggesting that Ni and Mo are not present as simple oxides but are instead incorporated into a polyoxometalate framework. Furthermore, the XRD patterns reveal that N_2 cold plasma bombardment does not induce any detectable changes in the diffraction peaks, indicating that the catalyst structure remains intact after treatment. Comparing the XRD patterns of the catalyst before and after MEO reaction (Fig. S12 in the Electronic Supplementary Material (ESM)), neither the peak intensity nor the peak shape exhibited any alteration. EPR characterization was carried out on the Ni-POM and Ni-POM-V_O catalysts (Fig. 1(c)). The higher intense peak of Ni-POM-V_O indicates that O atoms escape from the Ni–O–Ni bond after N_2 cold plasma bombardment, leading to the generation of a certain concentration of the V_O. The presence of a single Lorentz line and a *g* value of 2.003 indicate that unpaired electrons are still present in the as-prepared catalysts, further demonstrating the formation of rich oxygen vacancies [45–47].

Transmission electron microscopy (TEM) images (Figs. 2(a) and 2(c)) indicate that Ni-POM and Ni-POM-V_O lack distinct lattice stripes and are amorphous, consistent with the characteristics of polyoxometalates. Figures S1–S6 in the ESM present the SEM images and energy dispersive X-ray (EDS) spectra of the contrasting samples NiO and NiO-V_O, which exhibit nanoflower-like structures and a uniform distribution of oxygen and nickel elements. In Figs. 2(b) and 2(d), Ni-POM and Ni-POM-V_O consist of O, P, Ni and Mo with a uniform elemental distribution. The SEM and TEM images (Fig. S13 in the ESM) after the Ni-POM-V_O reaction also reveal a lumpy morphology, with elements such as O, P, Ni, and Mo still uniformly distributed. This indicates that the catalyst undergoes minimal alteration after long-term durability tests (48 h), demonstrating a certain degree of stability.

The nitrogen adsorption-desorption isotherms for all catalysts, shown in Fig. 3(a), are categorized as type IV isotherms, characterized by H3 hysteresis loops, which indicate mesoporous structures. A distinct hysteresis loop appears at elevated relative pressures ($P/P_0 > 0.9$) [48]. This behavior confirms the presence of mesopores in the catalyst structures, a crucial characteristic for applications requiring high surface areas and pore accessibility. A comparison of the specific surface areas of the catalysts (Table S1 in the ESM) reveals that NiO has the largest specific surface area (77.80 $m^2 \cdot g^{-1}$), due to its nanoflower structure, while MoO_3 has the smallest (19.87 $m^2 \cdot g^{-1}$), and Ni-POM has a specific surface area of 24.33 $m^2 \cdot g^{-1}$. Notably, the specific surface areas of NiO-V_O (69.84 $m^2 \cdot g^{-1}$) and MoO_3-V_O (19.87 $m^2 \cdot g^{-1}$) decreased relative to those of NiO (77.80 $m^2 \cdot g^{-1}$) and MoO_3 (19.87 $m^2 \cdot g^{-1}$). The specific surface area of Ni-POM-V_O increased to 31.54 $m^2 \cdot g^{-1}$. This may be due to plasma etching causing structural collapse in NiO and MoO_3 [49, 50], while Ni-POM-V_O only resulted in surface defects without structural damage, indicating greater stability. All catalysts exhibited remarkable consistency in average pore size, maintaining a mesoporous structure with pore sizes ranging from 2 to 30 nm (Fig. 3(b)).

The surface electronic states of Ni-POM-V_O catalysts were systematically investigated using X-ray photoelectron spectroscopy (XPS). The survey spectrum (Fig. S2 in the ESM) confirms the presence of Ni, O, and Mo as constituent elements in Ni-POM-V_O. Figure 4(a) presents the O 1s spectra of all catalysts, where the deconvoluted peaks at 529.4 (O_α), 531.0 (O_β), and 532.4 eV (O_γ)

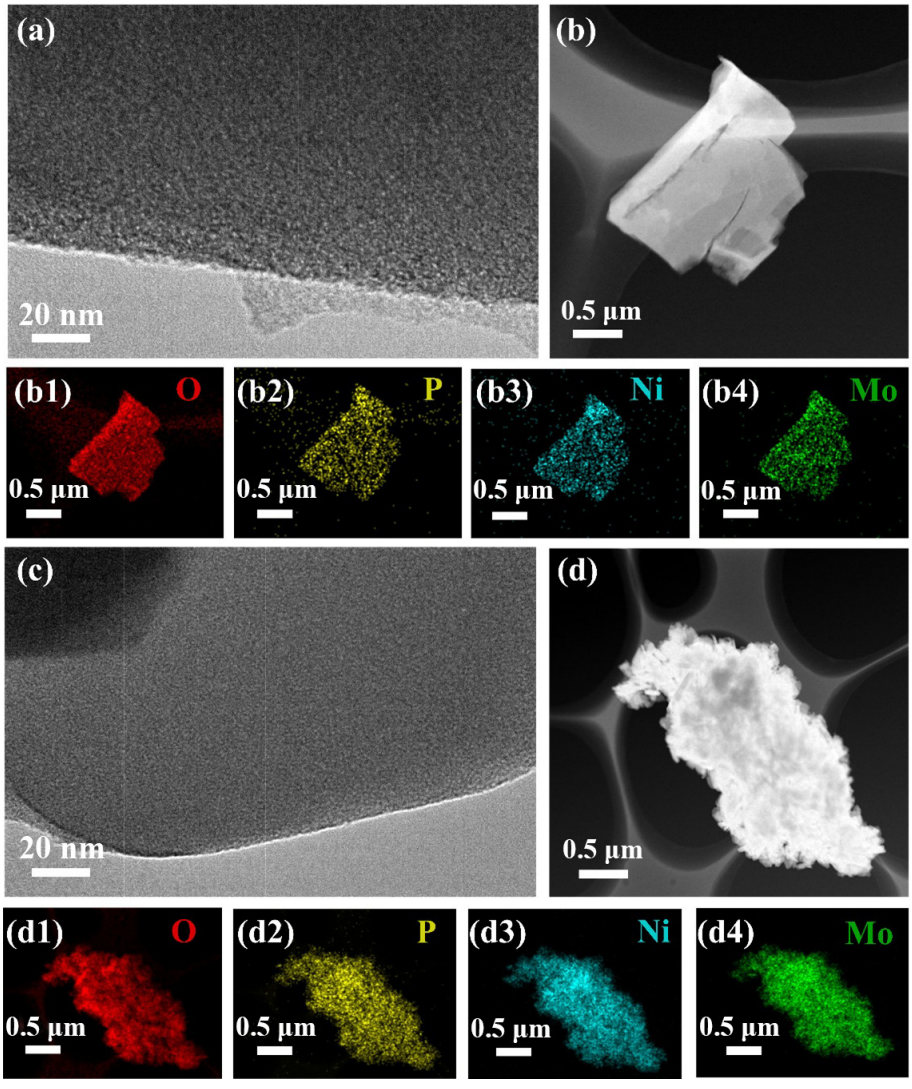

Figure 2 (a) and (b) TEM images and (b1)–(b4) EDS mapping of Ni-POM. (c) and (d) TEM images and (d1)–(d4) EDS mapping of Ni-POM-V_O.

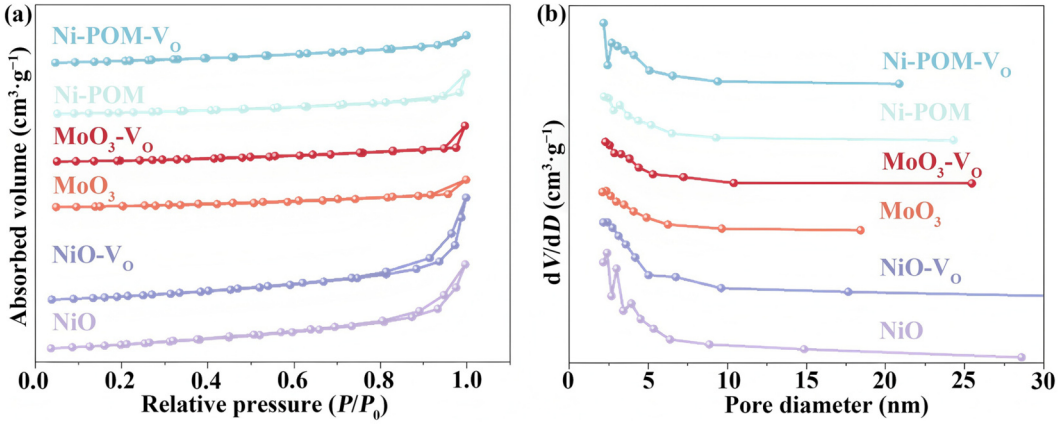

Figure 3 (a) N_2 adsorption–desorption isotherm and (b) pore width distribution of all catalysts.

correspond to lattice oxygen, oxygen vacancies, and adsorbed oxygen species, respectively [51, 52]. As quantified in Table S2 in the ESM, Ni-POM-V_O exhibits the highest concentration of oxygen vacancies among the studied catalysts. These vacancies play a crucial role in modulating the electronic structure of metal oxides by serving as active sites for molecular adsorption and activation, thereby reducing reaction energy barriers and enhancing catalytic efficiency. Notably, plasma etching treatment significantly increases the oxygen vacancy content, demonstrating a viable method for their controlled generation. Analysis of the post-reaction catalyst revealed a slight increase (91.29% to 92.44%) in oxygen vacancy content (Fig. S8 and Table S3 in the ESM). This increase resulted

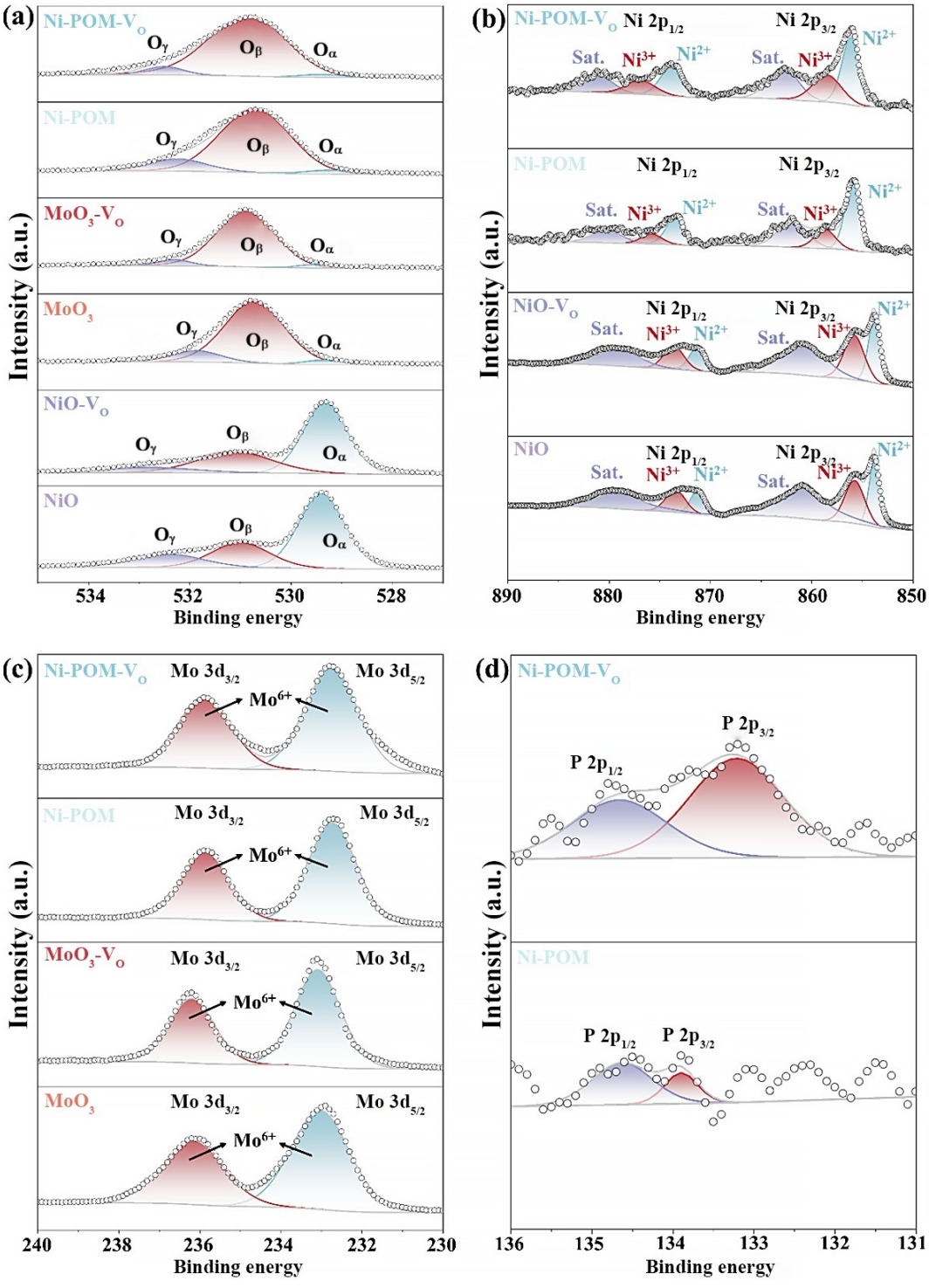

Figure 4 (a) O 1s XPS spectra of all catalysts. (b) Ni 2p XPS spectra of NiO, NiO-V_O, Ni-POM and Ni-POM-V_O. (c) Mo 3d XPS spectra of MoO_3 and MoO_3-V_O, Ni-POM and Ni-POM-V_O. (d) P 2p XPS spectra of Ni-POM and Ni-POM-V_O.

from redox reactions involving oxygen atoms in the metal oxide under the influence of an electric field, leading to the formation of oxygen vacancies [53]. This finding is consistent with the EPR (Fig. S11 in the ESM) test results obtained for the post-reaction catalyst. The Ni 2p spectra of NiO and Ni-POM-V_O (Fig. 4(b)) display characteristic spin-orbit doublets at 853.8 (Ni $2p_{3/2}$) and 871.2 eV (Ni $2p_{1/2}$), accompanied by satellite features at 860.0 and 879.5 eV, consistent with NiO [11]. In contrast, Ni-POM and Ni-POM-V_O exhibit positive binding energy shifts, suggesting electron density withdrawal from Ni centers due to the higher electronegativity of coordinating polyoxometalate ligands [54]. During the reaction process (Fig. S9 in the ESM), some Ni^{3+} (73.52% to 57.7%) was reduced to Ni^{2+} (24.48% to 42.3%). The Mo 3d spectra (Fig. 4(c)) reveal that MoO_3 and MoO_3-V_O exhibit primary emissions at 236.1 eV (Mo $3d_{3/2}$) and 233.0 eV (Mo $3d_{5/2}$), characteristic of Mo^{6+} [55, 56]. However, Ni-POM and Ni-POM-V_O show negative

binding energy shifts relative to MoO_3, indicating a reduced oxidation state of Mo [57]. This lower Mo oxidation state weakens metal-oxygen bonds, facilitating oxygen vacancy formation. The resultant vacancies provide additional charge storage sites and enhance ion insertion/extraction reversibility. Furthermore, increased oxygen vacancy concentration modifies the charge distribution in Ni-POM-V_O, improving its electronic conductivity and charge transfer capability. After participating in the electrochemical reaction, the oxidation state of Mo remains unchanged and continues to exist as Mo^{6+} (Fig. S10 in the ESM). The P 2p spectrum of Ni-POM-V_O (Fig. 4(d)) exhibits two components at 133.2 (P $2p_{3/2}$) and 134.7 eV (P $2p_{1/2}$), consistent with metal phosphate species [58].

The NH_3-TPD results, presented in Fig. 5(a) and Table S3 in the ESM, indicate weak acidic sites (< 300 °C), moderate acidic sites (300–500 °C), and strongly acidic sites (> 500 °C) [59]. The data indicate that NiO and NiO-V_O exhibit weak, moderate, and strong acidic sites, while MoO_3 and MoO_3-V_O display moderate and strong acidic sites. In contrast, Ni-POM and Ni-POM-V_O possess only moderate acidic sites. According to the table, Ni-POM (3.09 mmol·g^{-1}) and Ni-POM-V_O (3.53 mmol·g^{-1}) possess 20 times more moderate acidic sites than the other catalysts (NiO (0.13 mmol·g^{-1}), NiO-V_O (0.27 mmol·g^{-1}), MoO_3(0.12 mmol·g^{-1}), MoO_3-V_O (0.13 mmol·g^{-1})). Furthermore, the number of these sites increases in catalysts enriched with oxygen vacancies (Ni-POM-V_O). The detachment peaks of the moderately acidic sites are attributed to NH_3 binding with the Lewis acid centers. This finding suggests that oxygen vacancies are associated with Lewis acid sites [60]. The Lewis acidic active sites enhance the electrooxidation of H_2O and activate the adsorption of CH_4, resulting in the formation of two key intermediates: *OH and *CH_3 [61]. To assess the CH_4 adsorption capabilities of the catalysts, CH_4 temperature programmed desorption (CH_4-TPD) measurements were performed. As illustrated in Fig. 5(b) and Table S3 in the ESM, the CH_4-TPD curves can be categorized into three distinct regions: desorption of weak adsorption sites at temperatures below 200 °C, desorption of moderate adsorption sites between 200 and 500 °C, and desorption of strong adsorption sites at temperatures above 500 °C [62–64]. NiO and NiO-V_O possess three adsorption sites, exhibiting total adsorption quantities of 0.86 and 0.54 mmol·g^{-1}, respectively. In contrast, MoO_3 and MoO_3-V_O have two types of medium to strong adsorption sites, with total adsorption quantities of 0.14 and 0.10 mmol·g^{-1}, respectively. Notably, Ni-POM and Ni-POM-V_O are characterized by moderate adsorption sites only, with total adsorption values of 2.14 and 2.51 mmol·g^{-1}, respectively. Notably, methane adsorption on NiO-V_O and MoO_3-V_O decreased. This reduction can be attributed to structural collapse induced by plasma etching, which diminished their adsorption capacity. The methane adsorption capacity of Ni-POM-V_O exceeded that of Ni-POM due to the structural stability of Ni-POM-V_O, which is less prone to collapse. Additionally, the high concentration of Lewis acid favors methane adsorption and C–H bond activation.

3.2 Electrochemical performances of catalysts

The electrocatalytic performance of all catalysts for methane oxidation reaction (CH_4OR) was evaluated using a standard three-electrode H-cell setup in a 0.1 M KOH solution saturated with methane. Figure 6(a) illustrates distinct redox peaks for Ni-POM and Ni-POM-V_O within the voltage range of 1.0 to 2.0 V vs. RHE. A notable oxidation peak, occurring at 1.6 V, corresponds to the conversion of NiO to NiOOH [11]. As shown in Fig. S11 in the ESM, at a potential of 1.6 V, the current density of Ni-POM-POM-V_O in the presence of methane was significantly higher than that of the methane-free control group, indicating that methane participated in the oxidation reaction at this potential. Subsequently, the current density increases, indicating the electrooxidation of methane at the Ni-POM-V_O electrode. Figure 6(b) shows that the current density of CH_4OR on Ni-POM-V_O (8.73 mA·cm^{-2}) is double that of Ni-POM (4.37 mA·cm^{-2}) at 1.7 V vs. RHE, while no reaction occurs on the surface of other catalyst electrodes. This indicates that Ni-POM-V_O possesses superior catalytic activity for the CH_4OR. In Fig. 6(c), A lower R_{ct}

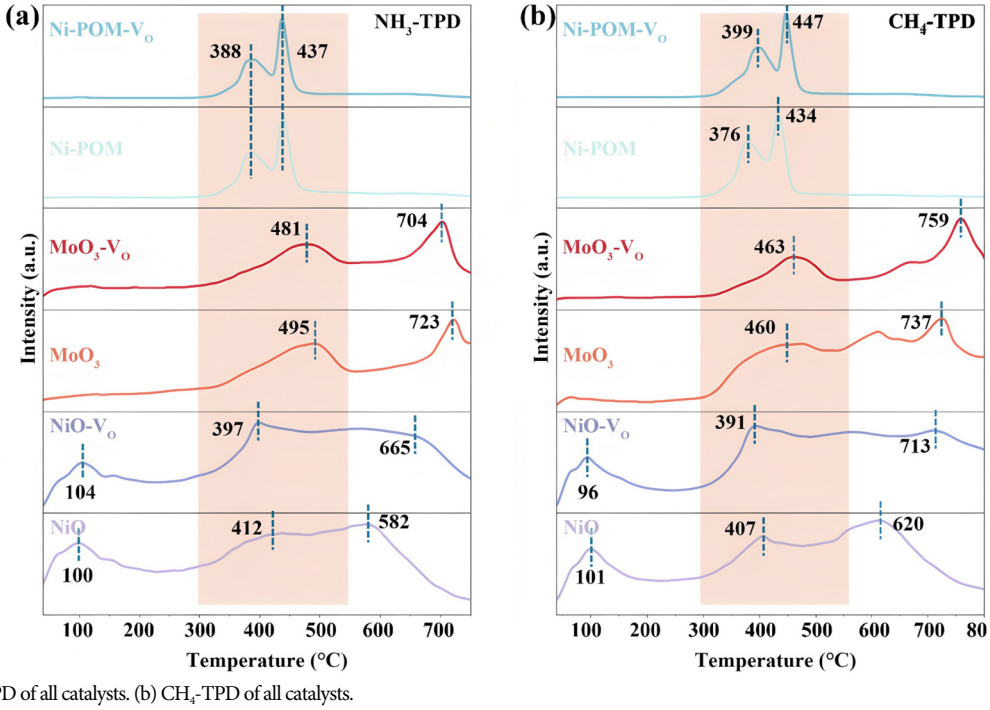

Figure 5 (a) NH_3-TPD of all catalysts. (b) CH_4-TPD of all catalysts.

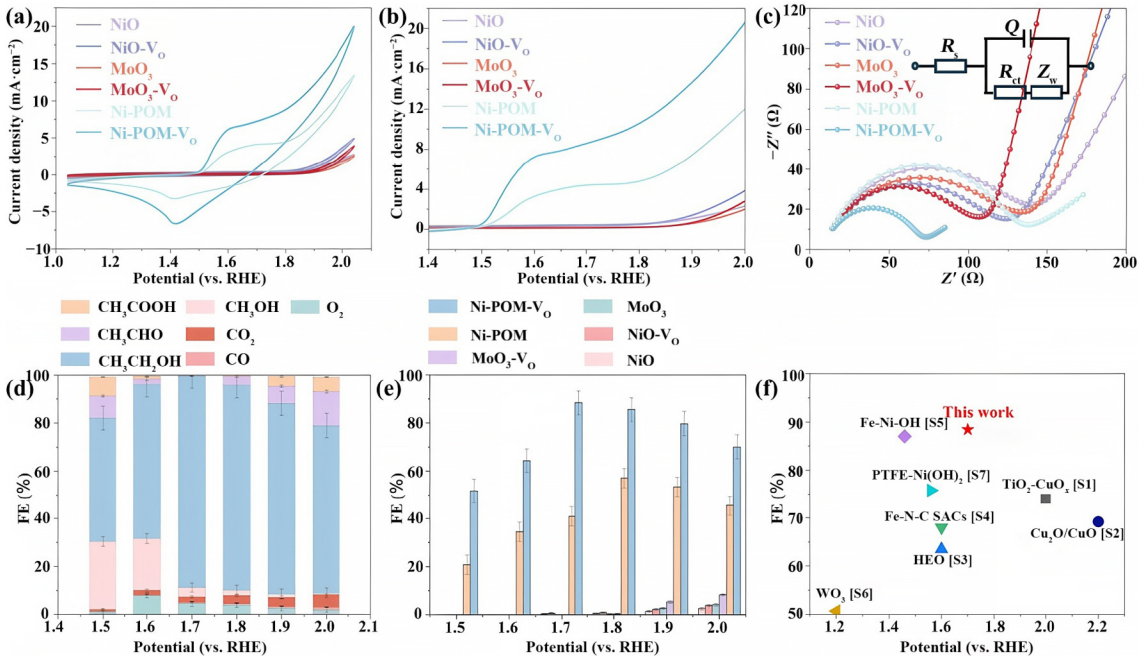

Figure 6 (a) CV of all catalysts in CH_4-saturated 0.1 KOH solution. (b) LSV of all catalysts. (c) Nyquist plots of all catalysts. (d) Faradic efficiency of different products of Ni-POM-V_O at different potentials (1.5–2.0 V vs. RHE). (e) Ethanol Faraday efficiency of different catalysts at different potentials (1.5–2.0 V vs. RHE). (f) The catalytic performance of the Ni-POM-V_O system in this study was compared with that of CH_4OR reported in the literature.

value indicates easier charge transfer and higher electrocatalytic activity of the catalyst. Specifically, Ni-POM-V_O (R_{ct} = 57.93 Ω) exhibits the smallest R_{ct}, demonstrating high electrocatalytic activity at 1.7 V vs. RHE. Ni-POM (R_{ct} = 94.04 Ω), NiO-V_O (R_{ct} = 102.3 Ω), NiO (R_{ct} = 116.4 Ω), MoO_3-V_O (R_{ct} = 88.4 Ω), and MoO_3 (R_{ct} = 115.6 Ω) exhibit larger R_{ct} values, corresponding to relatively lower electrocatalytic activity. This observation indicates a lower reactive charge transfer resistance from the electrode surface to the reactive molecules in CH_4OR [65]. Figure 6(d) illustrates the Faraday efficiency of Ni-POM-V_O for product formation across a voltage range of 1.5 to 2.0 V versus RHE. The maximum Faraday efficiency of 88.4% for ethanol production on the Ni-POM-V_O electrode was recorded at 1.7 V versus RHE. In Fig. 6(e), we further compare the Faraday efficiencies of ethanol production among various catalysts within the voltage range of 1.5 to 2.0 V vs. RHE. The results indicated that only Ni-POM-V_O and Ni-POM exhibited higher selectivity for ethanol. Furthermore, the selectivity of Ni-POM-V_O for ethanol was significantly higher than that of Ni-POM. This suggests that enhancing the concentration of Lewis acidity through oxygen vacancy modulation can improve ethanol selectivity. To investigate Ni-POM-V_O stability, inductively coupled plasma optical emission spectroscopy (ICP-OES) analysis data for the electrolyte were obtained. During leaching of Mo/Ni at a potential of 1.6–1.7 V vs. RHE in 0.1 M KOH solution, the following concentrations were measured: Ni (2.939 μg·L^{-1}), Mo (1261.598 μg·L^{-1}). Additionally, XPS (Figs. S9 and S10 in the ESM) and EDS (Fig. S13 in the ESM) data for the working electrode were supplemented. Combined with Table S3 in the ESM, these results confirm that under alkaline conditions, POM undergoes corrosion, Ni^{3+} is partially reduced to Ni^{2+}, while the valence state of Mo^{6+} remains unchanged. The primary configuration of the Ni-POM-V_O remains unchanged. As shown in Fig. 6(f) and Table S6 in the ESM, this catalyst exhibits superior Faraday efficiency for ethanol in the CH_4OR reaction compared to most previously reported results.

3.3 Reaction mechanism of CH_4OR

To investigate the impact of Lewis acids on CH_4OR, we performed DFT calculations on all catalysts to analyze potential reaction pathways (Figs. 7(a) and 7(b)). Firstly, the adsorption of CH_4 on the electrode surface is initiated via electron transfer, which results in the formation of $*CH_4$ (CH_4OR rate determining steps). The Gibbs free energy required to dissociate the C–H bond ($*CH_4$ chemical adsorption activation) on the Ni-POM-V_O surface (0.83 eV) was lower than those others catalysts. This finding suggests that Ni-POM-V_O more effectively promotes the activation and initiation of CH_4OR compared to Ni-POM. During the formation of $*CH_2$, the carbon atom of $*CH_3$ forms bonds with two low-coordinated Ni atoms adjacent to the Lewis acid site on the Ni-POM-V_O surface (0.64 eV). This interaction significantly reduces the dehydrogenation energy compared to Ni-POM (0.93 eV). For Ni-POM-V_O (−0.48 eV), the conversion from $*CH_2$ to $*CH_2OH$ occurs with significantly less energy than that for Ni-POM (0.10 eV). On the Ni-POM-V_O surface, $*CH_2$ subsequently migrates to the Lewis acid-containing POM site, where it reacts with *OH to form $*CH_2OH$ (Figs. 7(c) and 7(d)). POM significantly stabilizes the reaction intermediates ($*CH_3$, $*CH_2$, and $*CH_2OH$). Additionally, water (H_2O) is oxidized within the cavities of POM to generate *OH, which subsequently facilitates C–C coupling, promoting the formation and release of CH_3CH_2OH while inhibiting its oxidative conversion to CO_2 [26]. On the surface of Ni-POM-V_O (−0.95 eV), the reaction between $*CH_2OH$ and $*CH_3$ to form $*C_2H_5OH$ occurred with a lower energy barrier compared to Ni-POM (−0.10 eV). This lower barrier is conducive to C–C coupling and effectively explains the high selectivity for CH_3CH_2OH observed.

4 Conclusions

In conclusion, the electrochemical oxidation of CH_4 to ethanol was accomplished at ambient temperature and pressure, achieving a

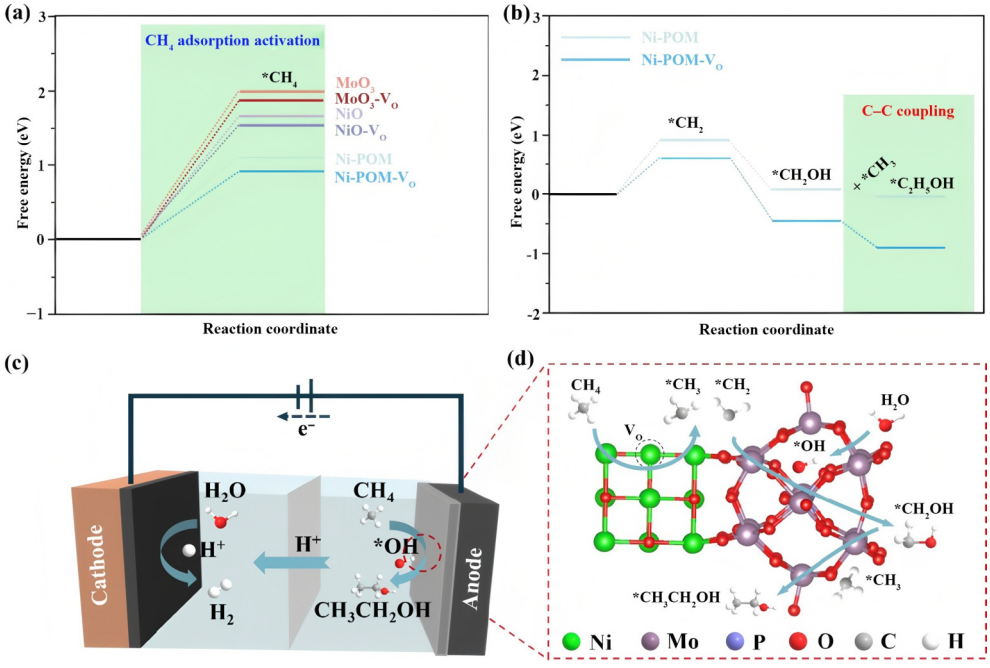

Figure 7 (a) Schematic diagram of a two-chamber electrolytic cell for the electrolysis of CH_4OR to produce ethanol. (b) Proposed reaction pathways for CH_4OR on the surface of Ni-POM-V_O. (c) Schematic diagram of a dual-cell electrolytic cell for producing ethanol via the electrolysis of CH_4OR. (d) Proposed reaction pathways for CH_4OR on the surface of Ni-POM-V_O.

selectivity of up to 88.4%. This was facilitated by Ni-POM, prepared through cluster-core co-assembly and subsequently etched with N_2 cold plasma, yielding Ni-POM-V_O enriched with oxygen vacancies. The presence of oxygen vacancies on Ni-POM-V_O led to the formation of numerous Lewis acid sites. These oxygen vacancy defects, exhibiting strong Lewis acid activity, facilitated the adsorption and activation of methane, leading to the formation of $*CH_2$ and $*CH_2OH$ intermediates. The intermediates $*CH_2$ and $*CH_2OH$ further adsorb onto polymetallic oxygenated groups (POM), promoting C–C coupling reactions that yield ethanol. This work provides a new method for adjusting the Lewis acid content on the catalyst surface through oxygen vacancies, improving the selectivity of methane electro oxidation to ethanol.

Electronic Supplementary Material: Supplementary material (SEM images, TEM image, and XPS relevant contents refer to Figs. S1–S7; BET, elemental valence content, NH_3-TPD, CH_4-TPD, and literature comparison relevant contents refer to Tables. S1–S4) is available in the online version of this article at https://doi.org/10.26599/NR.2026.94908604.

Data availability

All data needed to support the conclusions in the paper are presented in the manuscript and the Electronic Supplementary Material. Additional data related to this paper may be requested from the corresponding author upon request.

Acknowledgements

The authors thank the National Natural Science Foundation of China (No. 21902017), the China Postdoctoral Science Foundation (No. 2024M753166), Foundation of Technological Innovation and Application Development of Chongqing (No. CSTB2022BSXM-JCX0132), the Science and Technology Research Program of Chongqing Municipal Education Commission of China (No. KJQN202301121), and Natural Science Foundation of Sichuan of China (Nos. 2024NSFSC0295, 2024ZYD0157, and 2025NSFSC0999).

Declaration of competing interest

All the contributing authors report no conflict of interests in this work.

Author contribution statement

J. W. L.: Writing – original draft, methodology, investigation, data curation. Q. Z.: Writing – review & editing, writing – original draft, supervision, project administration, conceptualization. C. L. C.: Software, resources, methodology, investigation. S. J. Z.: Investigation, formal analysis, data curation. J. X. J.: Software, resources. J. Q. X.: Writing – review & editing, supervision, resources, conceptualization.

Use of AI statement

None.

References

[1] Qiu, H. Y.; Li, A.; Wang, Z. H.; Shangguan, Q. L.; Sun, Y. Z.; Tang, Y.; Wan, P. Y.; Jiang, H. M.; Chen, Y. M. Electrocatalytic methane conversion via *in-situ* generated superoxide radicals in an aprotic ionic liquid. *J. Colloid Interface Sci.* **2025**, *684*, 449–456.

[2] Jiang, S. Y.; Jiang, J. X.; Xiong, H. S.; Shang, S. Y.; He, G.; Zhang, Q. Recent progress in low-temperature electrooxidation catalysts for methane conversion. *Prog. Chem.*, in press, DOI: 10.7536/PC20251117.

[3] Kim, C.; Lee, J.; Lee, S.; Jung, W.; Min, H.; Choi, J.; Kim, S.; Kim, Y. T.; Lee, J.; Yoo, J. S. et al. High-selectivity room-temperature

partial oxidation of methane to methanol enabled by electrochemical oxygen promotion on IrO_2 catalysts. *Nat. Catal.* **2025**, *8*, 688–696.

[4] Xu, W. B.; Liu, H. X.; Hu, Y.; Wang, Z.; Huang, Z. Q.; Huang, C. D.; Lin, J.; Chang, C. R.; Wang, A. Q.; Wang, X. D. et al. Metal-oxo electronic tuning via *in situ* CO decoration for promoting methane conversion to oxygenates over single-atom catalysts. *Angew. Chem., Int. Ed.* **2024**, *63*, e202315343.

[5] Zhang, Q.; Peng, J. Y.; Xiong, H. S.; Jiang, S. Y.; Li, W.; Fu, X. H.; Shang, S. Y.; Xu, J. Q.; He, G. Cold plasma-activated Ni–Co tandem catalysts with CN vacancies for enhancing CH_4 electrocatalytic to methyl formate. *Appl. Catal. B: Environ. Energy* **2025**, *362*, 124759.

[6] Wang, Q. H.; Kan, M.; Han, Q.; Zheng, G. F. Electrochemical methane conversion. *Small Struct.* **2021**, *2*, 2100037.

[7] Yu, X.; Zholobenko, V. L.; Moldovan, S.; Hu, D.; Wu, D.; Ordomsky, V. V.; Khodakov, A. Y. Stoichiometric methane conversion to ethane using photochemical looping at ambient temperature. *Nat. Energy* **2020**, *5*, 511–519.

[8] Song, Q.; Xu, W. P.; Zeng, X.; Zhang, T. Q.; Hong, J.; Cullen, P. J. Electrochemical oxidation of methane to methylamine. *J. Am. Chem. Soc.* **2025**, *147*, 14966–14971.

[9] Wang, Q. H.; Li, T. F.; Yang, C.; Chen, M. H.; Guan, A. X.; Yang, L.; Li, S.; Lv, X. M.; Wang, Y. H.; Zheng, G. F. Electrocatalytic methane oxidation greatly promoted by chlorine intermediates. *Angew. Chem., Int. Ed.* **2021**, *60*, 17398–17403.

[10] Jiang, S. Y.; Zhang, Q.; Li, W.; Peng, J. Y.; Zhou, Y.; He, G. Electrocatalytic oxidation of methane to low-carbon alcohol via stable Ni^{+}/Ni^{0} interface. *Mol. Catal.* **2024**, *563*, 114234.

[11] Song, Y. F.; Zhao, Y. H.; Nan, G. Z.; Chen, W.; Guo, Z. K.; Li, S. G.; Tang, Z. Y.; Wei, W.; Sun, Y. H. Electrocatalytic oxidation of methane to ethanol via NiO/Ni interface. *Appl. Catal. B: Environ.* **2020**, *270*, 118888.

[12] Ma, Z. T.; Wang, Q. Y.; Liu, L. M.; Zhang, R. A.; Liu, Q. C.; Liu, P. G.; Wu, L. H.; Liu, C. Y.; Bai, Y.; Zhang, Y. D. et al. Low-coordination environment design of single Co atoms for efficient CO_2 photoreduction. *Nano Res.* **2024**, *17*, 3745–3751.

[13] Sun, C. T.; Liu, Y. R.; Lv, Z. H.; Liu, R.; Wang, C. L.; Li, L. H.; Wang, J. M.; Zhang, Y.; Yang, W. X.; Wang, B. Coordination-environment regulation of atomic Co–Mn dual-sites for efficient oxygen reduction reaction. *Nano Res.* **2024**, *17*, 6841–6848.

[14] Lin, J. M.; Mei, Z. B.; Guo, C. X.; Li, J. R.; Kuang, Y.; Shi, J. W.; Liu, J. J.; Li, X. P.; Li, S. L.; Liu, J. et al. Synthesis of isotypic giant polymolybdate cages for efficient photocatalytic C–C coupling reactions. *J. Am. Chem. Soc.* **2024**, *146*, 22797–22806.

[15] Cheng, D. M.; Li, K.; Zang, H. Y.; Chen, J. J. Recent advances on polyoxometalate-based ion-conducting electrolytes for energy-related devices. *Energy Environ. Mater.* **2023**, *6*, e12341.

[16] Koizumi, Y.; Yonesato, K.; Kikkawa, S.; Yamazoe, S.; Yamaguchi, K.; Suzuki, K. Small copper nanoclusters synthesized through solid-state reduction inside a ring-shaped polyoxometalate nanoreactor. *J. Am. Chem. Soc.* **2024**, *146*, 14610–14619.

[17] Shiels, D.; Brennessel, W. W.; Crawley, M. R.; Matson, E. M. Leveraging a reduced polyoxomolybdate-alkoxide cluster for the formation of a stable U(v) sandwich complex. *Chem. Sci.* **2024**, *15*, 11072–11083.

[18] Li, N.; Liu, J.; Dong, B. X.; Lan, Y. Q. Polyoxometalate-based compounds for photo- and electrocatalytic applications. *Angew. Chem., Int. Ed.* **2020**, *59*, 20779–20793.

[19] Du, L. L.; Li, Z.; Song, W. J.; Bao, Q. P.; Wang, P. F.; Gong, Z.; Zhang, Y. H.; Wu, Y. H.; Shi, F. N.; Zhou, M. D. et al. Polyoxometalate oxate solution: An electrolyte additive to sustainably improve the anodes electrode of aqueous Zn ion batteries. *Chem. Eng. J.* **2024**, *501*, 157743.

[20] Yan, P. F.; Wang, Q.; Wang, J. L.; Xu, H.; Yang, J. B.; Zhu, Y. H.; Chen, Q. L.; Mei, H.; Xu, Y. The first chiral polyoxometalate-based photocatalyst for highly efficient carbon dioxide reduction. *Chem. Eng. J.* **2025**, *507*, 160789.

[21] Jin, D. Y.; Qiao, F.; Zhou, Y.; Wang, J. F.; Cao, K. C.; Yang, J.; Zhao, J. K.; Zhou, L.; Li, H. T. Cu/Mo_2C synthesized through Anderson-type polyoxometalates modulate interfacial water structure to achieve hydrogen evolution at high current density. *Nano Res.* **2024**, *17*, 2546–2554.

[22] Lin, L. H.; Wei, F. F.; Jiang, R.; Huang, Y. C.; Lin, S. The role of central heteroatom in electrochemical nitrogen reduction catalyzed by polyoxometalate-supported single-atom catalyst. *Nano Res.* **2023**, *16*, 309–317.

[23] Wang, S. K.; Fung, V.; Hülsey, M. J.; Liang, X. C.; Yu, Z. Y.; Chang, J. Q.; Folli, A.; Lewis, R. J.; Hutchings, G. J.; He, Q. et al. H_2-reduced phosphomolybdate promotes room-temperature aerobic oxidation of methane to methanol. *Nat. Catal.* **2023**, *6*, 895–905.

[24] Wang, S. K.; An, H.; Hülsey, M. J.; Sun, G.; He, Q.; Yan, N. Sulfite-enhanced aerobic methane oxidation to methanol over reduced phosphomolybdate. *ACS Catal.* **2024**, *14*, 4352–4361.

[25] Chang, J. Q.; Wang, S. K.; Hülsey, M. J.; Zhang, S.; Nee Lou, S.; Ma, X. B.; Yan, N. Electrothermal conversion of methane to methanol at room temperature with phosphotungstic acid. *Angew. Chem., Int. Ed.* **2025**, *64*, e202417251.

[26] Nie, S. Y.; Wu, L.; Wang, X. Electron-delocalization-stabilized photoelectrocatalytic coupling of methane by NiO-polyoxometalate sub-1 nm heterostructures. *J. Am. Chem. Soc.* **2023**, *145*, 23681–23690.

[27] Yang, L.; Wang, C.; Dai, W. L.; Wu, G. J.; Guan, N. J.; Li, L. D. Progressive steps and catalytic cycles in methanol-to-hydrocarbons reaction over acidic zeolites. *Fundam. Res.* **2022**, *2*, 184–192.

[28] Xu, Q. C.; Wang, X. J.; Liu, Y.; Zhao, L. H.; Peng, F.; Ren, J. L. Unlocking precision in biomass conversion through functional ligand engineering of Lewis acidic MOFs. *Angew. Chem., Int. Ed.* **2025**, *64*, e202508256.

[29] Chen, Y. M.; Tang, S. S.; Li, L.; Liu, X. M.; Liang, J. Selective photocatalytic conversion of methane induced by Lewis acid-base pair on the surface of In_2O_3/TiO_2 heterojunction photocatalyst. *ACS Sustain. Chem. Eng.* **2023**, *11*, 3568–3575.

[30] Yue, Y. X.; Zuo, F. M.; Wang, B. L.; Xian, X. L.; Tang, J.; Zhang, H. F.; Zhang, Z. L.; Ke, Q. P.; Chen, W. Highly efficient catalyst for 1,1,2-trichloroethane dehydrochlorination via BN_3 frustrated Lewis acid-base pairs. *Nano Res.* **2024**, *17*, 4773–4781.

[31] Deng, Q.; Li, X.; Gao, R. J.; Wang, J.; Zeng, Z. L.; Zou, J. J.; Deng, S. G.; Tsang, S. C. E. Hydrogen-catalyzed acid transformation for the hydration of alkenes and epoxy alkanes over Co–N frustrated Lewis pair surfaces. *J. Am. Chem. Soc.* **2021**, *143*, 21294–21301.

[32] Qu, Q. Y.; Mao, Y.; Ji, S. F.; Liao, J. W.; Dong, J. C.; Wang, L. G.; Wang, Q. C.; Liang, X.; Zhang, Z. D.; Yang, J. R. et al. Engineering the Lewis acidity of Fe single-atom sites via atomic-level tuning of spatial coordination configuration for enhanced oxygen reduction. *J. Am. Chem. Soc.* **2025**, *147*, 6914–6924.

[33] Jin, H. Q.; Chen, X.; Da, Y. M.; Fan, L.; Jiang, R.; Xiao, Y. K.; Yao, B. Q.; He, Q.; Yu, Y.; Chen, W. Identifying the bifunctional mechanism in alkaline water electrolysis by Lewis pairs at the single-atom scale. *J. Am. Chem. Soc.* **2025**, *147*, 3874–3884.

[34] Chen, S. H.; Wang, B. Q.; Zhu, J. X.; Wang, L. Q.; Ou, H. H.; Zhang, Z. D.; Liang, X.; Zheng, L. R.; Zhou, L.; Su, Y. Q. et al. Lewis acid site-promoted single-atomic Cu catalyzes electrochemical CO_2 methanation. *Nano Lett.* **2021**, *21*, 7325–7331.

[35] Jing, R.; Lu, X. B.; Wang, J. F.; Xiong, J.; Qiao, Y. N.; Zhang, R.; Yu, Z. H. CeO_2-based frustrated Lewis pairs via defective engineering: Formation theory, site characterization, and small molecule activation. *Small* **2024**, *20*, 2310926.

[36] Zhu, Y. B.; Ma, Y. L.; Sun, Y. G.; Ji, W. X.; Wang, L. Q.; Lin, F.; Li, Y. Y.; Xia, H. Q. Synchronous construction of Ni/CeO_2/C with double defects as a dual engine for catalytic refinement of lignin oil under hydrogen-free condition. *ACS Catal.* **2024**, *14*, 17004–17013.

[37] Li, S. M.; Wu, Q. Y.; You, X. X.; Ren, X. F.; Du, P. L.; Li, F. Y.;

Zheng, N. F.; Shen, H. Anchoring frustrated Lewis pair active sites on copper nanoclusters for regioselective hydrogenation. *J. Am. Chem. Soc.* **2024**, *146*, 27852–27860.

[38] Kim, C.; Min, H.; Kim, J.; Moon, J. H. Boosting electrochemical methane conversion by oxygen evolution reactions on Fe–N–C single atom catalysts. *Energy Environ. Sci.* **2023**, *16*, 3158–3165.

[39] Li, A.; Qiu, H. Y.; Wang, Z. H.; Sun, Y. Z.; Tang, Y.; Wan, P. Y.; Jiang, H. M.; Chen, Y. M. Electrocatalytic conversion of methane to ethanol via promoted ·OH generation in aqueous electrolyte. *ACS Sustain. Chem. Eng.* **2024**, *12*, 9558–9567.

[40] Li, J. Y.; Luo, M. M.; Wang, M. L.; Ma, Y. Q.; Zheng, G. H.; Wang, M.; Zhou, Y. T.; Lu, Y. L.; Zhu, C. H.; Chen, B. Electrocatalytic conversion of methane to ethanol by ultrathin WO_3 nanosheets: Oxygen vacancy engineering. *Appl. Mater. Today* **2023**, *32*, 101855.

[41] Li, J. L.; Yao, L. B.; Wu, D. Z.; King, J.; Chuang, S. S. C.; Liu, B.; Peng, Z. M. Electrocatalytic methane oxidation to ethanol on iron-nickel hydroxide nanosheets. *Appl. Catal. B: Environ.* **2022**, *316*, 121657.

[42] Min, H.; Kim, C.; Lin, S. Y.; Choi, J.; Sim, Y.; Yu, B. Y.; Moon, J. H. Co-enriched high entropy oxides for efficient continuous electrochemical methane conversion: Catalytic performance and sustainability insights. *Adv. Mater.* **2025**, *37*, 2418767.

[43] Tian, H.; Yang, J. T.; Wang, X.; Jiao, H.; Gao, Z. F.; Zhu, K. Y.; He, Q.; Wang, Z. L. Ionic liquid-TiO_2–CuO_x composite interfaces combined with gas directional transmission for enhanced electrooxidation of methane to ethanol. *Appl. Catal. B: Environ. Energy* **2025**, *375*, 125411.

[44] Wang, R. M.; Tian, H.; Bian, L.; Bai, Y.; Liu, S. B.; Ma, Z.; Wang, Z. L. Tailoring the hydrophobicity of nickel hydroxide for selective electrooxidation of methane to methanol and ethanol. *Catal. Today* **2024**, *436*, 114734.

[45] Hu, X. Y.; Wang, J. T.; Wang, J.; Deng, Y.; Zhang, H. D.; Xu, T.; Wang, W. L. β particles induced directional inward migration of oxygen vacancies: Surface oxygen vacancies and interface oxygen vacancies synergistically activate PMS. *Appl. Catal. B: Environ.* **2022**, *318*, 121879.

[46] Liu, R. N.; Yan, Y. T.; Dun, L.; Yang, T. L.; Qin, B.; Wang, P. J.; Cai, W.; Liu, S. D.; Zheng, X. H. Oxygen vacancy-mediated high-entropy oxide electrocatalysts for efficient oxygen evolution reaction. *Mater. Today Catal.* **2025**, *8*, 100086.

[47] Gan, Y. H.; Cui, M. L.; Dai, X. P.; Ye, Y.; Nie, F.; Ren, Z. T.; Yin, X. L.; Wu, B. Q.; Cao, Y. H.; Cai, R. et al. Mn-doping induced electronic modulation and rich oxygen vacancies on vertically grown $NiFe_2O_4$ nanosheet array for synergistically triggering oxygen evolution reaction. *Nano Res.* **2022**, *15*, 3940–3945.

[48] Zhang, S. Y.; Li, X. S.; Li, K. X.; Ma, L.; Liu, H.; Li, S. T.; Dong, M. Z.; Ye, X. S. A controllable one-step millisecond synthesis of nanocrystalline mesoporous MgO with template-free by gliding arc plasma for efficient photocatalytic degradation of organic compounds. *J. Mater. Sci. Technol.* **2025**, *230*, 195–204.

[49] Cao, R. Y.; Zhou, J.; Wang, D.; Zhang, J. F.; Zhang, Y. Z.; Zhou, H. J.; Li, J. X. Improving capacitive deionization performance by using O_2 plasma modified carbon black. *Chem. Eng. J.* **2023**, *451*, 138530.

[50] Wang, J. M.; Cai, Z. Z.; Lin, D. X.; Chen, K.; Zhao, L. C.; Xie, F. Y.; Su, R.; Xie, W. G.; Liu, P. Y.; Zhu, R. Plasma oxidized $Ti_3C_2T_x$ MXene as electron transport layer for efficient perovskite solar cells. *ACS Appl. Mater. Interfaces* **2021**, *13*, 32495–32502.

[51] Jiang, H. R.; Zeng, C. H.; Zhu, W.; Luo, J. W.; Liu, Z. D.; Zhang, J. C.; Liu, R.; Xu, Y. H.; Chen, Y. N.; Hu, W. B. Boosting cycling stability by regulating surface oxygen vacancies of LNMO by rapid calcination. *Nano Res.* **2024**, *17*, 2671–2677.

[52] Su, J. H.; Yang, L.; Yu, D. B.; Dong, S. J. Exploring the potential of constructing a hybrid supercapacitor with FeCoNi-LDH porous material containing oxygen vacancies for high-performance energy storage applications. *Nano Res.* **2024**, *17*, 8134–8144.

[53] Guo, X. N.; Zhang, M. L.; Wang, W. Y.; Xie, Z. Y.; Lin, L. X.; Li, P. W.; Li, G. J.; Chen, Z.; Bo, S. H. Constructing oxygen vacancy-enriched Ag–$Mn(OH)_2$ via anionic leaching and Ag modification: Inducing high-valence Mn active sites for efficient electrocatalytic oxidation of 5-hydroxymethylfurfural. *Adv. Energy Mater.* **2025**, *15*, e02935.

[54] Zhao, Y. Q.; Wu, X.; Wang, H. L.; Ma, M.; Tian, J.; Wang, X. Phosphorus regulates coordination number and electronegativity of cobalt atomic sites triggering efficient photocatalytic water splitting. *Nano Lett.* **2024**, *24*, 16175–16183.

[55] Chi, J. Q.; Lin, J. H.; Qin, J. F.; Dong, B.; Yan, K. L.; Liu, Z. Z.; Zhang, X. Y.; Chai, Y. M.; Liu, C. G. A triple synergistic effect from pitaya-like $MoNi_x$–MoC_x hybrids encapsulated in N-doped C nanospheres for efficient hydrogen evolution. *Sustain. Energy Fuels* **2018**, *2*, 1610–1620.

[56] Zhao, X. Q.; Zhou, W. Q.; Xu, L. M.; Li, D. Q.; Huang, Z. A.; Zhang, M. M.; Li, Y. Z.; Hao, X. J.; Xu, J. K. Oxygen-vacancy Ce–MoO_3 nanosheets loaded Pt nanoparticles for super-efficient photoelectrocatalytic oxidation of methanol. *Appl. Surf. Sci.* **2024**, *655*, 159576.

[57] Mao, J. J.; Li, X. X.; Huang, Y.; Zhu, C. Y.; Yu, F. S.; Cheng, F. Nanorod-assembled urchin-like molybdenum-manganese oxide heterostructure with enhanced oxygen vacancies as a cathode for quasi solid state zinc-ion batteries. *J. Mater. Chem. A* **2025**, *13*, 9222–9232.

[58] Wu, G. Z.; Chen, H. J.; Wang, D. H.; Zhang, Y.; Xu, J. Chemistry evolution of $LiFePO_4$–$NaHSO_4 \cdot H_2O$ system during roasting and recovery of Li and Fe. *J. Alloys Compd.* **2024**, *1007*, 176376.

[59] Shao, Y. W.; Sun, K.; Zhang, L. J.; Xu, Q.; Zhang, Z. M.; Li, Q. Y.; Zhang, S.; Wang, Y.; Liu, Q.; Hu, X. Balanced distribution of Brønsted acidic sites and Lewis acidic sites for highly selective conversion of xylose into levulinic acid/ester over Zr-beta catalysts. *Green Chem.* **2019**, *21*, 6634–6645.

[60] Mao, R. X.; Li, F. Y.; Bu, Y. Z.; You, W. J.; Li, J. Q.; Qi, J. M.; Pu, L. Y.; Ning, P.; Ma, Y. X.; Wang, X. Q. Efficient catalytic decomposition of ozone by flake NiFe-LDH with multiple acidic sites. *Appl. Surf. Sci.* **2025**, *700*, 163191.

[61] Tian, H.; Zhang, Z. Y.; Fang, H.; Jiao, H.; Gao, T. T.; Yang, J. T.; Bian, L.; Wang, Z. L. Selective electrooxidation of methane to formic acid by atomically dispersed CuO_x and its induced Lewis acid sites on V_2O_5 in a tubular electrode. *Appl. Catal. B: Environ. Energy* **2024**, *351*, 124001.

[62] Osti, A.; Costa, S.; Rizzato, L.; Senoner, B.; Glisenti, A. Photothermal activation of methane dry reforming on perovskite-supported Ni-catalysts: Impact of support composition and Ni loading method. *Catal. Today* **2025**, *449*, 115200.

[63] Chen, F.; Zhou, H. Y.; Liu, D. D.; Qin, X.; Jing, Y. C.; Chen, L. Y.; Shi, R.; Liu, Y. N.; Zhang, J. G.; Zhu, Y. F. et al. Defective ZnO nanoplates supported AuPd nanoparticles for efficient photocatalytic methane oxidation to oxygenates. *Adv. Energy Mater.* **2024**, *14*, 2303642.

[64] Hao, S. Y.; Xue, Y. Y.; Peng, C.; Mi, Y. Y.; Yan, Y. Q.; Wang, M. Y.; Han, Q.; Zheng, G. F. Photocatalytic CH_4-to-ethanol conversion on asymmetric multishelled interfaces. *J. Am. Chem. Soc.* **2024**, *146*, 25870–25877.

[65] Zhang, Q.; Wang, J. L.; Guo, F.; He, G.; Yang, X. H.; Li, W.; Xu, J. Q.; Yin, Z. Y. Nitrogen cold plasma treatment stabilizes Cu^0/Cu^+ electrocatalysts to enhance CO_2 to C2 conversion. *J. Energy Chem.* **2023**, *84*, 321–328.